Influence of Si addition on the corrosion behaviour of 9 wt.% Cr ferritic/martensitic steels exposed to oxygen-controlled molten Pb-Bi eutectic at 550 and 600 °C

Hao Shi [a,b,*], Hui Wang [c,d,*], Renate Fetzer[a], Annette Heinzel[a], Alfons Weisenburger[a], Kangli Wang[b], Adrian Jianu[a], Georg Müller[a]

[a] *Institute for Pulsed Power and Microwave Technology (IHM), Karlsruhe Institute of Technology (KIT), Hermann-von-Helmholtz-Platz 1, 76344 Eggenstein-Leopoldshafen, Germany*

[b] *State Key Laboratory of Advanced Electromagnetic Engineering and Technology, School of Electrical and Electronic Engineering, Huazhong University of Science and Technology, Wuhan 430074, PR China*

[c] *Science and Technology on Reactor Fuel and Materials Laboratory, Nuclear Power Institute of China, Chengdu, Sichuan 610041, PR China*

[d] *School of Mechanical Engineering, Chengdu University, Chengdu 610106, PR China*

* Corresponding author. E-mail address: hao.shi@kit.edu (H.Shi); qinghe5525@163.com (H. Wang).

Keywords: Ferritic/martensitic steel; LBE; Corrosion; Silicon addition; Electron microscopy.

Abstract

Three 9 wt.% Cr ferrite/martensite steels (two alloyed with Si) have been exposed to oxygen-controlled LBE at 550 and 600 °C, respectively. The passivating oxide scale consists of a spinel layer plus internal oxidation zone (IOZ). By adding Si, the thickness of spinel layer is decreased while the IOZ is enhanced. Moreover, a Si-rich oxide layer is observed underneath the spinel layer on Si-containing samples after 2000 h exposure at 600 °C. Besides, the less visible cracks/exfoliations on Si-containing samples indicate the positive role of Si addition on scale adherence.

1. Introduction

The promising thermo-physical, thermo-hydraulic and neutronic properties of heavy liquid metals like Pb or Pb-Bi eutectic (LBE) render them as attractive heat transfer or storage mediums for the advanced energy production systems, like Gen-IV liquid metal cooled fast reactors, accelerator driven systems (ADS), fusion reactors, concentrated solar power (CSP) [1-7]. However, structural materials often suffer from severe degradation, especially corrosion attacks, when in contact with heavy liquid metals [1, 8-10]. Moreover, the corrosion attack is aggravated when the operation temperature is above 500 ℃ [9-13]. By dissolving certain amount of oxygen in heavy liquid metal, it is able to passivate an oxide layer on steel surface as a corrosion barrier [8-10]. Moreover, the corrosion resistance of steels (ferritic, austenitic steels) can be further improved by adding the passive oxide layer forming elements such as Al or Si [11-12, 14-19].

Among the various material solutions, a type of modified 9 wt.% Cr ferritic/martensitic (F/M) alloyed with Si (≤ 1.5 wt.%), also called SIMP steel, has been developed targeting for the liquid metal

environment applications [20-24]. Previous exposure tests of these steels in oxygen-saturated LBE indicate the improved corrosion performance and mechanical properties when compared with T91 (Fe-9Cr-0.9Mo-0.5Mn, wt.%) [20-21, 23]. For instance, Wang et al. [20] studied the corrosion behaviour of SIMP steels (Si content varies from 0 to 1.43 wt.%) in oxygen-saturated LBE at 550 ℃, and Shi et al. [21] compared the corrosion performance of a SIMP steel (alloyed with 1.43 wt.% Si) with T91 in oxygen saturated LBE at 600 °C. All of the tested specimens are able to form a triple oxide layer structure at both temperatures, which consists of an outer layer of $PbO{\cdot}xFe_2O_3$ and Fe_3O_4, an inner layer of spinel-type $FeCr_2O_4$, and an internal Cr-oxidized zone [20-21]. Samples alloyed with Si have formed oxides precipitates like Fe_2SiO_4 and SiO_2 in the spinel layer which help reduce the growth rate of oxide layer. However, no continuous Si-rich oxide layer is observed. In addition, investigations of thermal stability of SIMP steels show the relatively high thermal stability and unchanged tensile properties even after 2000 h aging at 550 ˚C [22]. Although new formed Fe_2W type Laves precipitates after 5000 h aging increase the strength of Si-containing steels, the ductility of all tested samples is not degraded.

Moreover, tensile tests of the SIMP steel (1.4 wt.% Si) indicate that the candidate material shows a slight decrease in strength (from 358 MPa to 346 MPa) and elongation (from 44% to 28%) after 2000 h exposure to molten LBE at 600 ˚C [23]. The lower temperature (200 to 450 ˚C) tensile tests of SIMP steel (1.4 wt.% Si) also display the sensitivity to liquid metal embrittlement (LME) [24]. However, the LME of F/M steels only happens at certain conditions, like direct contact between liquid metal and steel, loading stress and the exposed temperature close to the melting point of LBE (~350 ˚C) [1, 25-27]. Moreover, the LME effect can be mitigated by a fast strain rate or an initial protection layer [28-29].

Previous corrosion tests of SIMP steels are only performed in oxygen saturated conditions. The relatively high oxygen amount dissolved in oxygen saturated Pb/LBE not only promote the fast oxidation of steels, but also increase the risk for Pb/Bi being oxidized [30-31]. Therefore, an optimized oxygen concentration of 10^{-7}-10^{-4} wt.% has been defined in the temperature range of 400 to 600 ˚C [30]. Numerous corrosion tests of steels in liquid Pb/LBE show the applicability of the proposed oxygen concentration either in stagnant or flowing conditions [9-11, 15, 32-33]. Therefore, the motivation of this research work is to study the corrosion behaviour of SIMP steels in a relatively low oxygen containing LBE environment (≤ 10^{-6} wt.% oxygen concentration) at 550 and 600 ˚C. Besides, the influences of Si content, different exposure temperature and time on the corrosion/oxidation behaviour of candidate steels will be discussed.

2. Materials and methods

2.1 Sample preparation

Three steels with varying Si content are prepared by vacuum induction melting. Each cylindrical sample (diameter: 90 mm, height: 100 mm) is forged into a sheet with a final thickness of 20 mm. During the forging process, the temperature is kept above 900 °C. Then, specimens are hot-rolled with 74.8% reduction of thickness at 1100 °C, followed by a second hot rolling with 48.4% reduction of thickness at 950 °C. The total thickness reduction is 87% for all samples. After rolling, the samples are heat treated at 1030 °C for 1 h and quenched in water. Finally, the sheets are tempered at 720 °C for 1.5 h with air cooling. Table 1 gives the chemical compositions of prepared steels, as measured by EDX. Minor additions of other elements are C<0.12 wt.%, Ta<0.1 wt.% and Zr<0.01 wt.%.

Table 1 Chemical composition of main elements added in 9 Cr F/M steels, measured with EDX (wt.%).

Code	Fe	Si	Cr	Mn	W	V
0Si	Bal.	0	8.5	0.3	2.0	0.3
0.7Si	Bal.	0.7	8.6	0.4	2.5	0.2
1.0Si	Bal.	1.0	8.4	0.4	2.3	0.2

The samples are firstly ground using by 1200, 2400 grit paper and polished, and then etched with an acid solution (a mixture of 400 ml ethyl alcohol, 50 ml HCl, 50 ml HNO_3, 6 g Picric acid) for 90 s. Fig. 1 displays the surface morphologies of all samples after etching. All samples exhibit the typical martensite lath structures with grain sizes of around 10 to 20 μm. In addition, both Si-free (0Si) and Si-containing (0.7Si, 1.0Si) samples have formed bright and Cr-rich nano-sized precipitates along the grain boundaries. These precipitates are reported as $Cr_{23}C_6$ [21, 23]. The large precipitates observed in Fig. 1 (b) are impurities from SEM sample preparation.

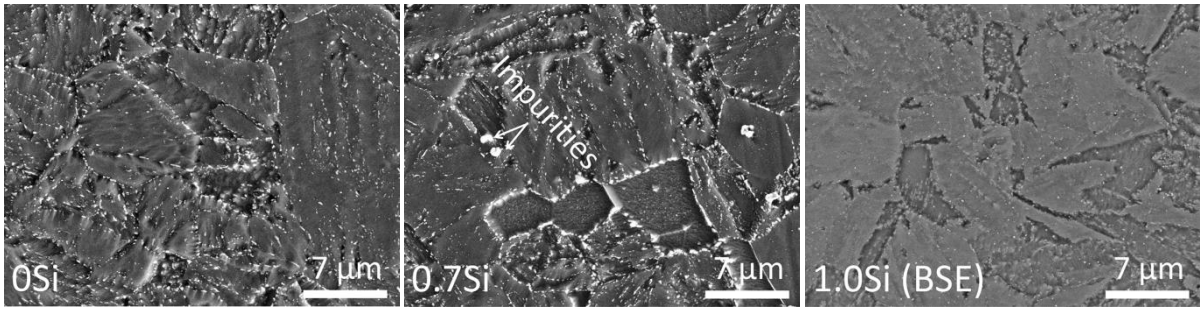

Fig. 1 SEM images of the microstructure in the bulk material of 0Si, 0.7Si, and 1.0Si steels.

2.2 Corrosion tests

The corrosion tests are performed in a stagnant molten Pb/PbBi corrosion facility, called COSTA (**CO**rrosion test stand for **ST**agnant liquid **A**lloys in KIT) [11]. Samples are cut in rectangular pieces with a dimension of 10 mm*20 mm, and a thickness of 1.5 mm. A 1.5 mm hole is drilled in each sample near one edge. All specimens are ground with 1200 grit paper, cleaned with acetone and ethanol in an

ultrasonic bath and dried. Then, each sample is fixed with a Mo-wire to an alumina holder to prevent floating during corrosion test and hanged in an alumina crucible containing the molten LBE. The oxygen concentration in LBE is adjusted to 10^{-6} wt.% at both 550 and 600 °C, which is estimated based on the saturation data in the reference [1]. The oxygen content in the liquid Pb was controlled via the H_2/H_2O ratio in the gas phase. The oxygen activity of the gas phase was measured at the outlet of the quartz-tube with an oxygen sensor and displayed as oxygen partial pressure [8, 30]. The oxygen partial pressure in the gas phase above the molten LBE is monitored and kept constant during the measurement. For each exposure temperature, two samples from the same composition are immersed into one alumina crucible with 200 g molten LBE. One sample from each composition is extracted after 1000 h while the other is extracted after 2000 h.

The general process for the corrosion experiments have been described in literature [11-12]. After the corrosion tests, samples are extracted from molten LBE using a glove box (to keep the oxygen condition close to one in the furnace) and cooled down to ambient temperature. The remaining adherent Pb/Bi on the sample surface is cleaned by immersing the exposed sample into a liquid solution of acetic acid, hydrogen peroxide and ethanol (1:1:1) [11, 34].

2.3 Characterization methods

The oxide layers and microstructures of all samples have been characterized using Scanning Electron Microscopy (SEM, model: Hitachi S-4800 and Zeiss LEO 1530 VP), equipped with electron dispersive X-ray spectroscopy (EDX). The applied high voltage of the electron beam was varied from 10 to 20 kV keeping a working distance of 9 mm. In case of cross section analysis, a Ni-layer (~25 µm) is electroplated beforehand to avoid spallation of oxide layer caused by mechanical grinding. Then, the samples are embedded in resin, and ground with sand papers, e.g. surface finish of 1200 #, 2400 #, followed by polishing with diamond paste up to 1 µm particle size. Before conducting the SEM/EDS measurement, a thin palladium (Pd) layer is sputtered on the specimen surface.

Phase compositions have been characterized by X-Ray Diffraction (XRD, Seifert PAD II) with Cu Kα1 radiation (λ=0.15406 nm, 40 kV and 30 mA) in Bragg–Brentano geometry (θ-2θ) with a step size of 0.02° and a scan speed of 0.1 °/min.

3. Results

3.1 XRD characterization

At 550 °C, $FeCr_2O_4$, Cr_2O_3 and Ferrite (from bulk alloy) are the main phases detected on all three compositions (0Si, 0.7Si and 1.0Si), independent of the exposure time. An aditional signal from PbBiO is identified on 1.0Si sample. The XRD results after 2000 h exposure are depicted in Fig. 2 (a). When

the temperature is increased to 600 °C, a difference in phase compositions is observed comparing the Si-free and Si-containing samples. The phases identified on 0Si sample (1000h and 2000 h) are $FeCr_2O_4$ and BCC (weak) while the phases detected on 0.7Si (1000h and 2000 h) and 1.0Si sample (2000 h) comprise of $FeCr_2O_4$, Fe_2SiO_4, BCC and PbO. Although the difference in peak positions between $FeCr_2O4$ and $FeSi_2O4$ is less than 1°, it is still able to identify them. For instance, the 2θ of $FeCr_2O4$ at 30.15° (220), 35.54° (311), 43.17° (400), 53.54° (422), 57.06° (511), 62.67° (440), while the 2θ of Fe_2SiO_4 with the same miller index is 30.3°, 35.68°, 43.37°, 53.82°, 57.37°, 63.01°. Besides, the wide peaks obtained by X-ray diffraction also reflect overlapped diffraction signals. The weak signal of BCC on 0Si sample indicates the large thickness of oxide layer formed. The phase identified on 1.0Si sample (1000 h) includes Fe_3O_4, $FeCr_2O_4$ and BCC. As an example, the XRD results of 1.0Si sample (1000 h) and all samples after 2000 h exposure are displayed in Fig. 2 (b).

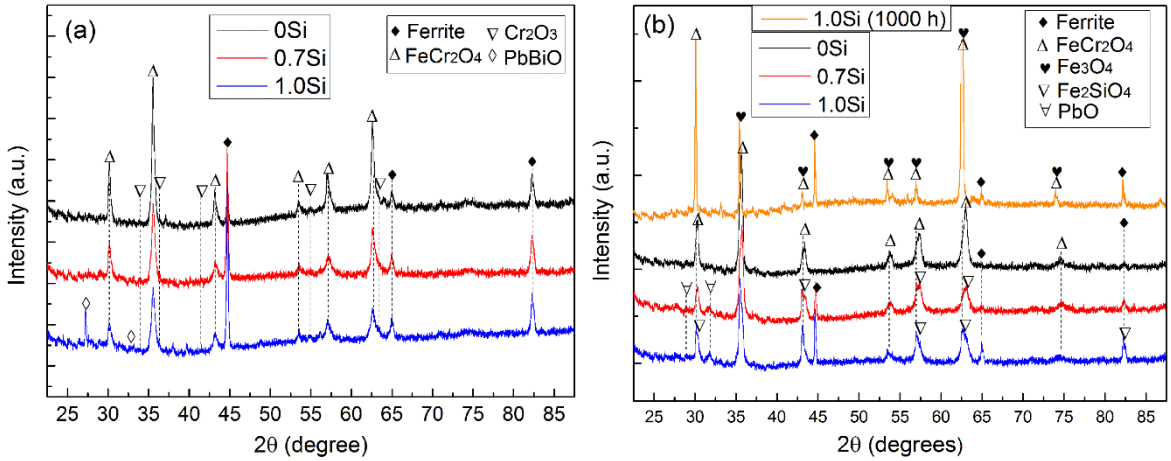

Fig. 2 XRD spectra of samples (0Si, 0.7Si, 1.0Si) after exposure to 10^{-6} wt.% oxygen-controlled LBE, (a): exposed at 550 °C for 2000 h; (b): exposed at 600 °C for 1000 h (1.0Si, orange colored line) and 2000 h (all samples).

3.2 Surface morphologies

Fig. 3 shows the surface morphologies of all samples after 1000 h and 2000 h exposure at 550 °C. The SEM surface profile of 0Si sample (1000 h) shows the formation of a dense and thick oxide scale. Parts of the oxide scale, accounting for 10% of the surface area, show the evidence of oxide scale exfoliation. However, no corrosion/dissolution attack is observed at regions of oxide scale spallation. Besides, some cracks are also visible on the surface oxide layer. EDX measurement of the surface layer indicates the enrichment of Fe, Cr and O. The surface of the 0.7Si sample is also covered by a protective oxide layer. No corrosion attack or oxide scale exfoliation has been observed. Some micro-cracks are also observed at high magnification, but less visible than on the 0Si sample. According to the EDX analysis, the oxide layer is mainly enriched in Fe, Cr and O. The measured Si content is around 1.5 wt.% (accelerating voltage: 10 kV). The sample 1.0Si exhibits similar oxide scale morphologies as that observed on 0.7Si sample. However, micro-cracks are not observed. The Si content measured from sample surface is around 2.0 wt.% (10 kV).

Compared with the sample after 1000 h exposure, 0Si sample (2000 h) has formed a more stable oxide layer with only a few spots of spallation (< 5% surface area), see also in Fig. 3. The micro-cracks

observed after 1000 h exposure are still visible after 2000 h exposure, although they become less obvious. The sample doped with Si (0.7Si) has formed a rough surface layer. The bright contrast regions are rougher than the dark regions. According to the EDX analysis, the bright area contains some Pb and Bi rich precipitates. Besides, the micro-cracks are also visible here. Three spots show the evidences of oxide scale exfoliation. The sample with 1.0Si has formed an oxide layer with a morphology similar that of the 0.7Si sample. However, no micro-crack or oxide layer exfoliation is observed. EDX measurements indicates the enrichment of O, Cr and Fe, while the Si concentration shows no difference between the oxide layer and bulk material.

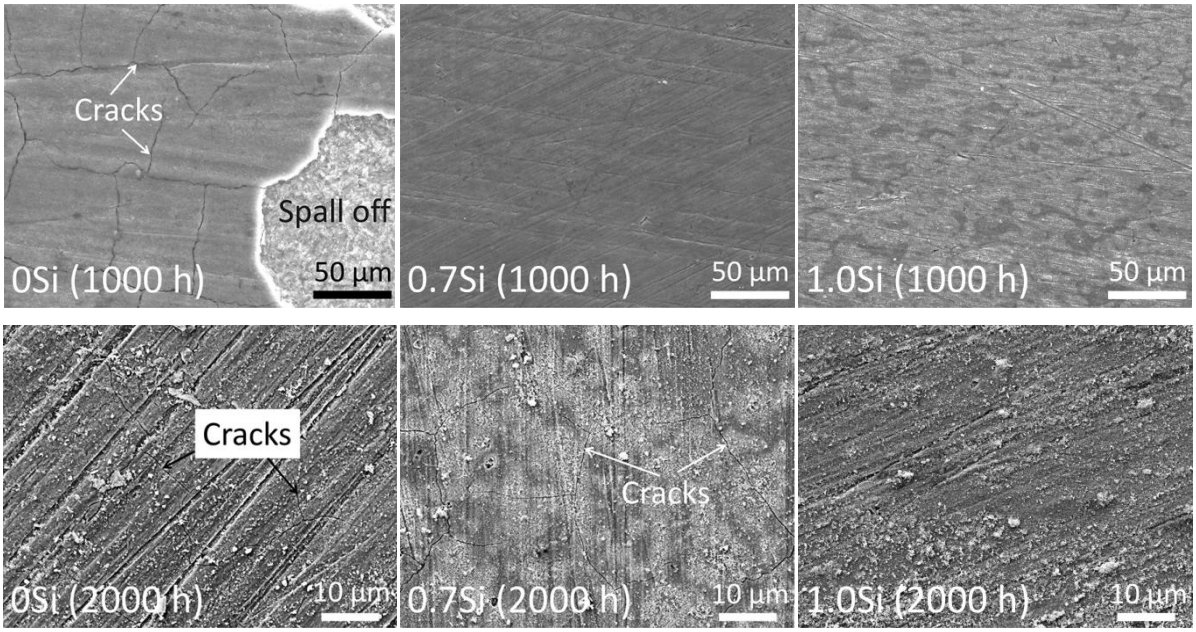

Fig. 3 Surface morphologies of samples (0Si, 0.7Si, 1.0Si) after 1000 h and 2000 h exposure to 10^{-6} wt.% oxygen-controlled LBE at 550 °C.

Fig. 4 displays the surface morphologies of samples after 1000 h and 2000 h exposure at 600 °C. The surface of 0Si sample is covered by a protective oxide scale without corrosion attack or oxide layer exfoliation. EDX measurement reveals the enrichment of O, Cr and Fe on the surface. Besides, a few micro-cracks are also observed on the surface layer. The 0.7Si has also formed a protective oxide scale that is enriched in O, Cr and Fe. Besides, some areas show darker contrast (around 15-20% surface area). EDX measurement of these areas reveal nearly two times higher concentrations of Si and Cr compared to the general surface oxides. In addition, micro-cracks are widely observed in the surface layer. At the 1.0Si sample, a different surface morphology is observed. Instead of forming a uniform oxide layer, a Fe-rich oxide layer has formed with spots of localized spallation of the scale over the entire surface. EDX measurements of dark pore regions, where the Fe-rich oxide layers are missing, reveal the enrichment of O, Cr and Fe, indicating the formation of Fe-, Cr-rich oxide layer. Considering the XRD results (Fig. 2 (b)), the Fe-rich layer is assigned to magnetite while the dark pore regions have formed a Fe-Cr spinel.

After 2000 h exposure, the 0Si sample has also formed a uniform oxide layer without spallation. But, the micro-cracks become more visible comparing with the sample after 1000 h exposure. The chemical compositions measured by EDX remains unchanged with increasing the exposure time,

mainly being enriched in O, Cr and Fe. In contrast, the oxide scale formed on 0.7Si sample displays different aspects concerning roughness. According to EDX analysis, the smooth part is enriched in O, Cr and Fe while the rough part contains less Cr and more Fe. The concentration of Si is lower than 1 wt.% and is the same at both the smooth and rough surface. In addition, a higher concentration of Pb and Bi is detected at the rough surface regions. Moreover, these rough regions also display the formation of small pores, marked at the image. Cracks are also visible at the entire surface, but less frequent when compared with the Si-free sample. The surface of 1.0Si sample shows all the characteristics that were observed on 0.7Si sample. However, a higher Si concentration, around 3 wt.%, is detected at the surface layer. Besides, the cracks become even less frequent in comparison with 0.7Si sample, and as well the pores are more rarely observed at the rough surface part.

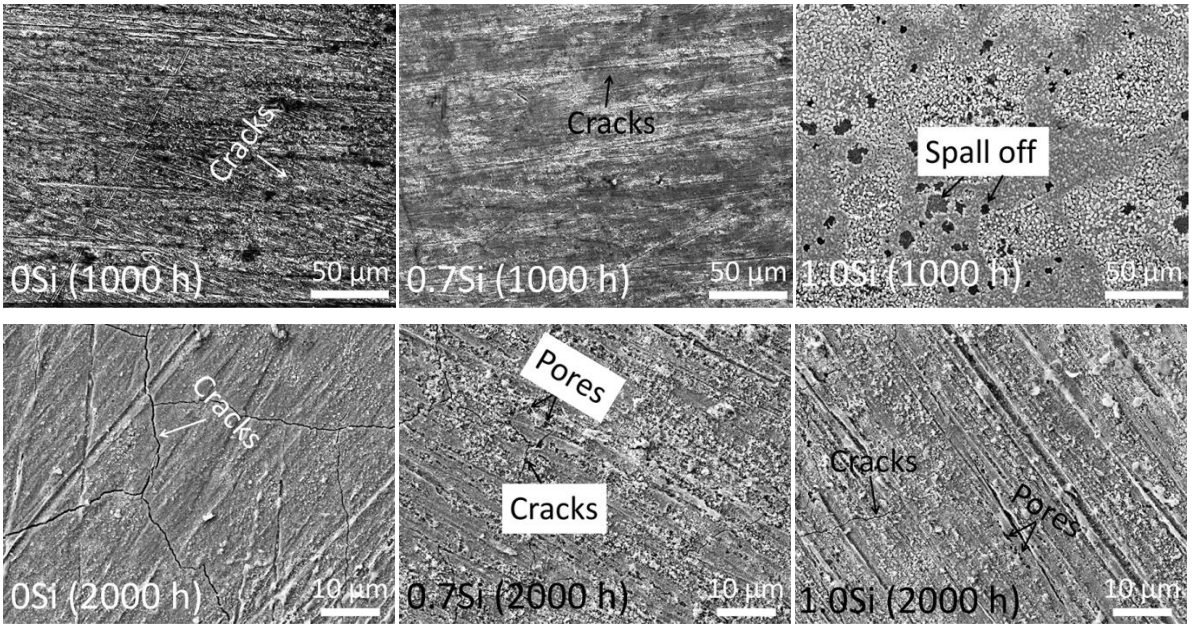

Fig. 4 Surface morphologies of samples (0Si, 0.7Si, 1.0S) after 1000 h and 2000 h exposure to 10^{-6} wt.% oxygen-controlled LBE at 600 °C.

3.1.3 Cross section analysis

Exposed at 550 °C

The oxide layers formed on all the samples (0Si, 0.7Si and 1.0Si) at the different exposure times show similarities in microstructures and composition, namely a spinel layer plus an internal oxidation zone (IOZ). The only difference is the thickness of the spinel layer and IOZ due to the effects of Si addition and prolonged exposure time. As an example, the cross sections of the samples with longest exposure time (2000 h) are shown in Fig. 5. Here, only two samples 0Si and 1.0Si are presented since sample with 0.7Si shows a very similar oxide scale microstructure as the 1.0Si sample.

Fig. 5(a) shows the SEM cross section as well as EDX elemental line scan profiles of exposed 0Si sample. According to the image, the spinel layer passivating on steel surface displays a dense upper layer and an inner layer with pores and microcracks, which are typical morphologies observed on T91

[33]. The cracks observed from surface pass through the upper dense part. Below the spinel layer, some oxide roots penetrating into the bulk alloy have formed the IOZ, marked on the image (Fig. 5(a)). Based on the EDX line scan, the upper part of spinel layer is enriched in O, Cr and Fe. As the measurement reaches to the inner layer, the signal of Cr increases and reaches to the maximum value at the interface of spinel layer/IOZ. In case of the IOZ, the intensity of O decreases significantly when compare with the spinel layer while the signal of Fe is stronger in IOZ. EDX analysis reveals the preferential oxidation of Cr in IOZ, which indicates the formation of Cr_2O_3 according to the XRD result (Fig. 2 (a)).

Fig. 5(b) exhibits the cross section image as well as EDX analysis of 1.0Si sample. Generally, the spinel layer displays a similar morphology like the 0Si sample: an upper dense part plus an inner porous part. However, the entire spinel layer is much thinner compare with one of the Si-free sample, whereas the IOZ is much larger, almost two times thicker than at the 0Si sample. According to the EDX measurement, coincided signals of O, Cr and Fe are observed at the spinel layer. The signal of Cr increases at the interface of porous layer/IOZ, indicating the formation of Cr_2O_3 precipitates. However, the signal of Si does not show any difference between the spinel layer and alloy matrix. In the IOZ, strong O signal coincided with signals of Cr and Si have been detected at the dark roots, representing the formation of Cr- and Si- rich oxides. However, the Si-rich oxides are not detected by XRD due to the low amount and the distance to the surface.

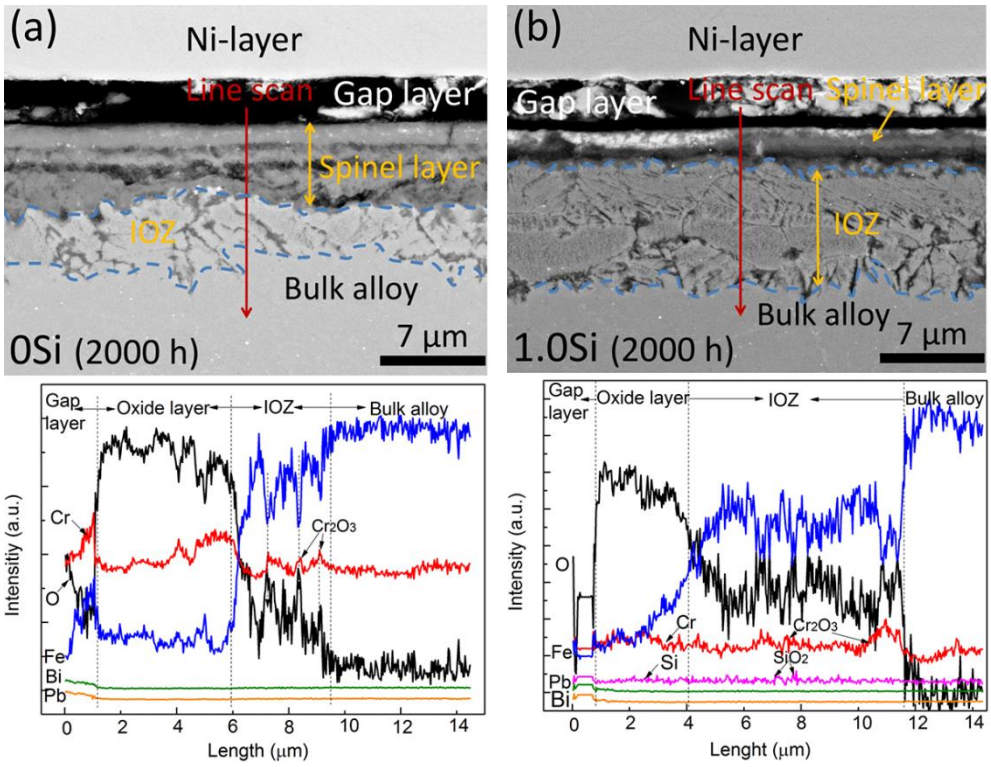

Fig. 5 Line scan profiles of 0Si (a) and 1.0Si (b) samples after 2000 h exposed to 10^{-6} wt.% oxygen-containing LBE

at 550 °C

Based on the measured value, the spinel layer thickness, IOZ and total oxidized region (spinel layer plus IOZ) are plot as a function of Si content in Fig. 6. Data obtained from both 1000 h and 2000 h exposure are considered. Since the measured oxide scale thickness varies at different regions, ten different regions are measured and an average value is applied to clarify the oxide scale evolution. First the data after 1000 h exposure are analyzed. According to the plot, the thickness of spinel layer decreases by adding Si. The minimum thickness is obtained with the 0.7Si sample. However, the small thickness of spinel layer formed on 1.0Si is comparable to that of the 0.7Si sample when considering the variation of the oxide scale thickness. The IOZ shows an almost linear increase with Si content. The total oxidized zone is also increased as the amount of Si increases. Similarly, samples after 2000 h exposure also display a significant reduction in the thickness of spinel layer by adding Si. Like the samples after 1000 h exposure, the 0.7Si sample has formed the thinnest spinel layer. In addition, all samples display an increased thickness of the spinel layer by prolonging the exposure time. However, the Si-free sample shows the largest increase of spinel layer, more than 2 times while Si-containing samples show a relatively low growth rate, which accounts for a 10% to 20% times thicker scale after 2000 h exposure. Regarding the IOZ after 2000 h exposure, a linear relation with Si content is obtained as well. However, the thickness of IOZ only increases slightly for all samples after 2000 h exposure, independent of Si addition. Compared with the samples after 1000 h exposure, 0Si sample has shown a significant increase in total oxidized zone after 2000 h exposure, while samples with Si addition only increase slightly in oxide scale thickness with prolonged exposure time.

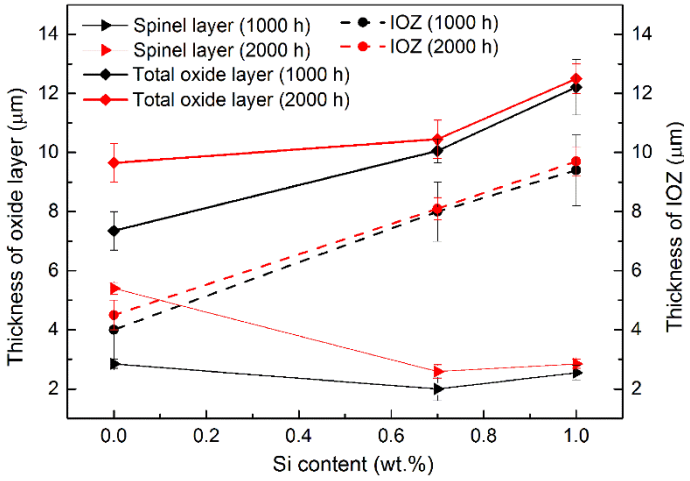

Fig. 6 Plot of thickness of spinel layer, IOZ and total oxide layer as a function of Si content (wt.%) when exposed to 10^{-6} wt.% oxygen-containing LBE at 550 °C, the error bar represents the measured minimum and maximum thickness of the oxide layer.

Exposed at 600 °C

A spinel layer and an IOZ is formed on three of the samples, similar to the samples after exposure to 550 °C hot LBE, namely 0Si (1000 h & 2000 h), 0.7Si (1000 h). The other samples show a different corrosion/oxidation behaviour, namely the 1.0Si (1000 h & 2000 h), 0.7Si (2000 h). The cross sectional

images of these samples are displayed in Fig. 7. The 1.0Si (1000 h) sample has formed a duplex oxide layer, consisting of a discontinuous outer layer of magnetite plus an inner spinel layer. The IOZ occurs in some regions additionally. The pores formed by oxide scale spallation (Fig. 4) are also visible from the cross section. They penetrate only the magnetite layer. The 0Si sample (2000 h) has formed a similar oxide layer structure as that observed at 550 °C (Fig. 5). The other two samples (0.7Si (2000 h) and 1.0Si (2000 h)) have partially formed a thin and dense Si-rich oxide layer underneath the spinel layer, which was not observed after exposure at 550 °C. XRD analysis only shows the evidence of $FeSi_2O4$. However, SiO_2 might also form at this temperature range. It is difficult to be identified due to its low amount and amorphous structure [20, 35]. Therefore, this Si-rich layer is described as a $FeSi_2O4$ and SiO_2 containing layer.

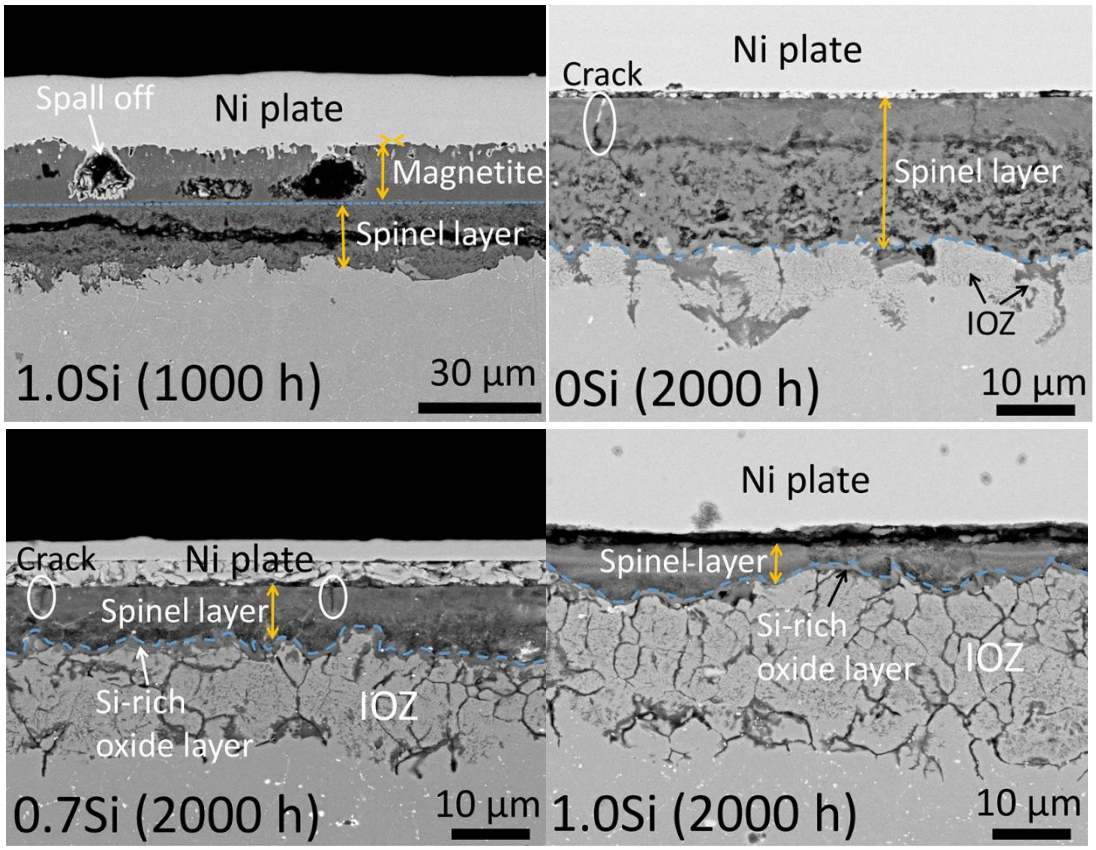

Fig. 7 Cross section images of 1.0Si (1000 h), 0Si (2000 h), 0.7Si (2000 h) and 1.0Si (2000 h) after exposed to 10^{-6} wt.% oxygen-controlled LBE at 600 °C, Si-rich oxide layer ($FeSi_2O_4$ and SiO_2)

In addition to the general corrosion/oxidation behaviour shown in Fig. 7, two further morphologies are observed on 1.0Si sample (2000 h), shown in Fig. 8. The type I (Fig. 8(a)) consists of an oxide layer (spinel plus Si-rich oxide layer) without IOZ or with a very thin IOZ (less than 1 µm). The morphologies of this oxide layer look similar to the oxide layer formed in general region (Fig. 7, 1.0Si (2000 h)). However, the Si-rich oxide layer is continuous in contrast to the discontinuous $FeSi_2O_4/SiO_2$ layer observed at general region. The thickness of the entire oxide scale is comparable to the spinel layer formed at most of the parts, around 6 to 8 µm. According to the EDX analysis, both the signals of

Cr and Si increase at the inner layer and the maximum value of Si is observed at the interface of oxide scale/alloy matrix, which is exactly located at the inner dense layer part, marked in Fig. 8 (a). This result confirms the formation of Si-rich oxide layer. The type II shown in Fig. 8(b), which is also visible at some regions of 0.7Si (2000 h), is the formation of a thick spinel layer plus IOZ. The thickness of the spinel layer varies in a large range, from 15 to 21 µm. Most of the spinel layer, especially close to the inner part, is porous. These porous layers reflect the pores observed from the surface (Fig. 4: 0.7Si, 1.0Si). The $FeSi_2O_4/SiO_2$ layer observed in other regions (general region and type I layer) is invisible here. Below the oxide layer, a large IOZ with thickness around 20 µm is observed.

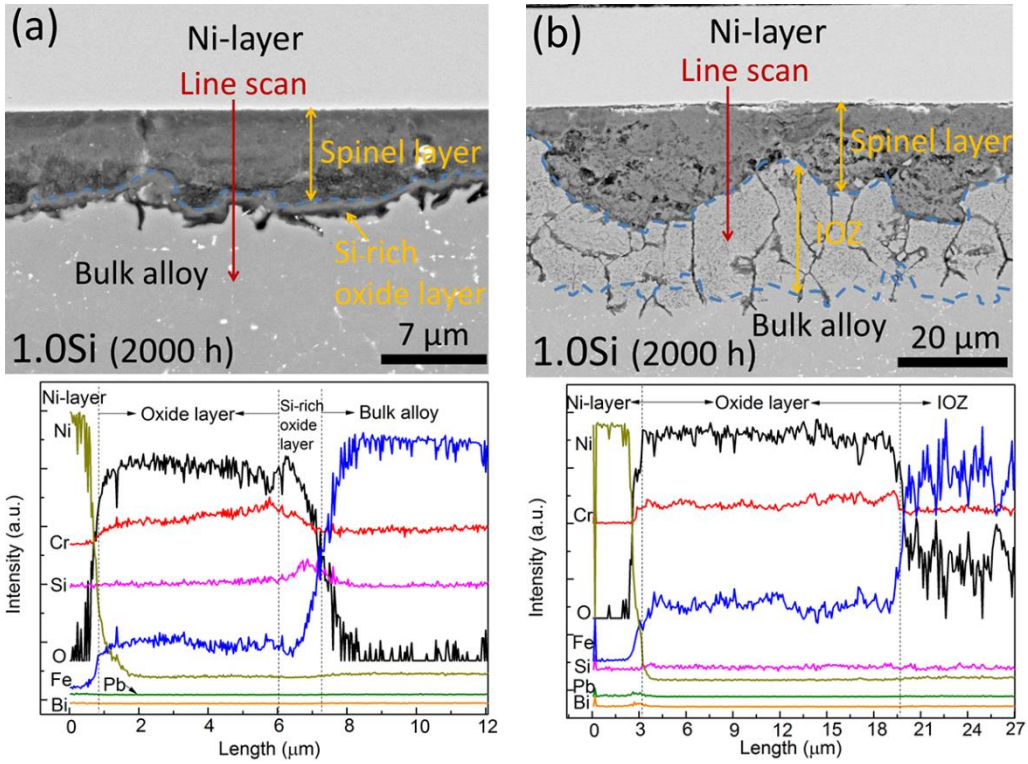

Fig. 8 Line scan profiles of 1.0Si sample after 2000 h exposed to 10^{-6} wt.% oxygen-containing LBE at 600 °C, (a): formation of Si-rich oxide layer ($FeSi_2O_4$ and SiO_2), without IOZ; (b): formation of thick spinel layer and IOZ, without Si-rich oxide layer.

Fig. 9 displays thickness of spinel layer, IOZ and total oxidized zone (oxide layer plus IOZ) as a function of Si content when exposed to 600 °C. Since sample 1.0Si after 1000 h exposure has formed a duplex layer of Fe_3O_4 and $FeCr_2O_4$, it is not considered for the plot. For the other samples with partially deviating oxide scale microstructure, 0.7Si (2000 h) and 1.0Si (2000 h), only the most observed regions (Fig. 7) are considered for the plot. According to the results, the thickness of spinel decreases while the IOZ increases by adding Si after 1000 h exposure. The total oxidized zone shows a slight decrease but is comparable between the 0Si and 0.7Si samples. After 2000 h exposure, samples (0.7Si and 1.0Si) have formed thinner spinel layer compared with 0Si sample. The average thickness of the IOZ tends to increase by adding Si. Unlike the samples exposed to 550 °C, the total oxidized zone of candidate steel is decreased by adding Si at 600 °C. Although 0.7Si sample has shown the minimum

thickness, a deviation of the average value exists. The thinner oxide layer formed on Si-containing samples might be attributed to the formation of the Si-rich oxide layer.

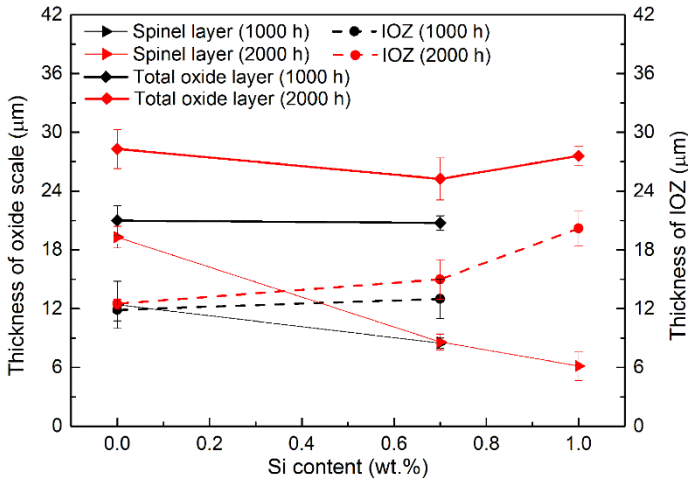

Fig. 9 Plot of thickness of spinel layer, IOZ and total oxide layer as a function of Si content (wt.%) when exposed to 10^{-6} wt.% oxygen-containing LBE at 600 °C, the error bar represents the measured minimum and maximum thickness of the oxide layer.

4. Discussion

The samples tested in 10^{-6} wt.% oxygen-containing molten LBE (current study) have shown the oxidation behaviour different from that exposed to oxygen-saturated conditions (oxygen concentration in LBE: ~2 x 10^{-3} wt.% [21]). Instead of forming triple-layer structure (Fe_3O_4-$(Fe,Cr)_3O_4$-IOZ), double-layer structure ($(Fe,Cr)_3O_4$-IOZ) is obtained with the lower oxygen content. One possible explanation for the different oxidation behaviour might be related to the different oxygen concentration in LBE. According to the thermo-dynamic calculation [8, 36], the oxygen concentration applied in the current study is higher than the threshold for the stability of Fe_3O_4 (around 10^{-8} -10^{-7} wt.%), but quite close to it. However, the value is much higher than the stability limit of $(Fe,Cr)_3O_4$ (around 10^{-11}-10^{-10} wt.%). Therefore, the $(Fe,Cr)_3O_4$ layer is able to be stabilized during the exposure. But the formation of Fe_3O_4 layer is still possible, as shown by the magnetite layer observed on 1.0Si sample after 1000 h exposure at 600 °C. Besides, another possible reason resulting in the formation of only $(Fe,Cr)_3O_4$ layer can be that due to the relatively large surface area of exposed samples (around 400 mm^2 in one crucible), the oxygen supply from the gas phase might be insufficient (due to the limited diffusion rate of oxygen coming from the cover gas into the liquid LBE), resulting in a decrease of the oxygen concentration in the LBE below the stability limit of magnetite. The oxygen concentration and supply are still large enough to promote the formation of a single spinel layer. Such kind of oxide scale structure is also observed by other researchers either due to the lower oxygen concentration or the introduced flowing conditions (instability of Fe_3O_4 layer), namely, stagnant corrosion exposure of 1.5 wt.% Si containing T91 in 10^{-8} to 10^{-7} wt.% oxygen containing LBE at 550 ℃ [19], corrosion tests of T91 in flowing LBE at 550 °C with 10^{-7} and 10^{-6} wt.% dissolved oxygen [10, 33], corrosion test of steel

E911 in 10^{-6} wt.% flowing oxygen-containing LBE at 550 °C [36], corrosion of 9Cr-3Si steels in 10^{-7}-10^{-6} wt.% oxygen-containing flowing Pb-Bi eutectic at 450 and 550 °C [37].

Compared with Si-free samples, low amount of Si addition (≤ 1.0 wt.%) improves the corrosion resistance of candidate materials by decreasing the thickness of spinel layer. At 550 ˚C, the oxidation of Si and Cr at the interface of spinel/IOZ and internal oxidation of both elements along grain boundaries retard the outward diffusions of Fe and Cr, and slow down the spinel formation. Although this mechanism is also adapted to the Si-containing samples exposed to 600 °C, an additional effect of Si addition exists at 600 °C. The investigations of Si-containing samples at 600 °C (2000 h exposure) prove the formation of an inner $FeSi_2O_4/SiO_2$ layer, which can impede the oxidation process. Moreover, the formation of a dense Si-rich oxide layer on higher Si-containing steel (1.0 wt.% Si) can even inhibit the inner permeation of oxygen, avoiding the formation of IOZ. As the thickness of spinel layer increases with increasing exposure time, the oxygen partial pressure at the spinel/bulk alloy interface will be reduced. Besides, the higher temperature exposure promotes the outward diffusion of alloying elements like Si. Therefore, it is possible to promote the formation of Si-rich oxide layer at 600 °C (2000 h exposure) due to the high oxygen affinity of Si [8, 32, 38].

On the other hand, the internal oxidation is enhanced by Si addition. In case of Si-free sample, the internal oxidation is mainly due to the oxidation of Cr. However, the internal oxidation zone of Si-containing samples is a mixture of Cr- and Si- rich oxides. This is mainly due to the high oxygen affinity of both Cr and Si, which can oxidize at a relatively low oxygen activities or partial pressure [8]. Moreover, the lowest oxygen dissociation partial pressure of SiO_2 allows Si to be oxidized in a larger depth when compared with Si-free sample. Besides, the thickness of IOZ also increases with the exposure time and temperature.

Regarding the influence of Si addition on the oxide scale adherence, the exfoliation of oxide scale seems to be impeded by Si addition when the samples were exposed to 550 °C. At 600 °C, no evidence of oxide scale spallation is observed on Si-free sample. However, the cracks observed on the oxide scale surface become less visible by increasing Si amount, in spite of the temperature and exposure time. Since the spinel layer thickness is decreased by adding Si, the thermal stress formed during oxide scale growth is decreased [39]. Therefore, less cracks are observed on Si-containing samples. Moreover, the pores observed at the interface of spinel layer and IOZ, induced by outward diffusion of Fe and Cr, reduce the bonding strength and might result in the oxide scale exfoliation. Therefore, the thinner the formed spinel layer, the less outward diffusion of Fe and Cr, and accordingly the less pores are formed. This might explain the positive influence of Si addition on the oxide scale adherence.

In addition, the exposure time and temperature also influence the oxidation behaviour of

candidate steels. Comparing the samples with different exposure time but at same temperature, the thickness of spinel layer formed on Si-free sample increases 100% by doubling the exposure time, while Si-containing samples increase less than 50%, see in Fig. 6 and Fig. 9. This might also indicate the positive role of Si in reducing the grow rate of spinel layer. As for the IOZ, the exposure time shows less effect on either Si-free or Si-containing samples. When comparing the samples exposed at different temperatures but same exposure time (e.g. 2000 h), the Si-free sample has shown the larger increase of spinel layer thickness by increasing the temperature from 550 °C to 600 °C, when compared with Si-containing samples, shown in Fig. 10. It means that the temperature has a significant influence on the oxidation rate of Si-free sample. Regarding the temperature effects on IOZ, all of the samples have shown a large increase of IOZ as the exposure temperature increases from 550 to 600 °C.

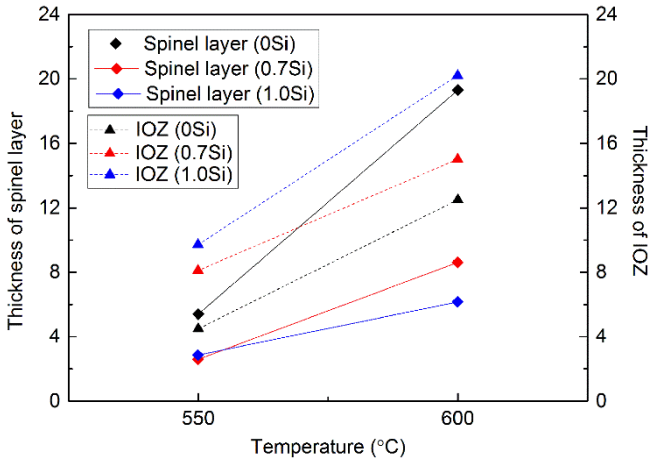

Fig. 10 Evolution of thickness of spinel layer and IOZ as a function of exposure temperature after 2000 h exposure, 0Si, 0.7Si and 1.0Si samples.

The Si-free 9 wt.% Cr F/M steel investigated in this study involves a relatively high oxidation rate, especially when the temperature reaches 600 °C. The formation of thick Fe-, Cr-rich spinel layer not only increases the risk of oxide scale exfoliation, but also reduce the heat transfer of base material [1, 40]. Alloying with Si (≤ 1.0 wt.%) results in some positive effects, namely a reduced spinel layer thickness, low amounts of crack formation, slow growing Si-rich oxide layer etc. However, the internal oxidation is enhanced. The total thickness of oxidized zone is actually increased (except regions without IOZ). The formation of inner Si-rich oxide layer is only partially observed on 0.7Si and 1.0Si samples after 2000 h exposure at 600 °C. These results indicate that the proposed Si concentrations (< 1.0 wt%) is still insufficient to promote the formation of a continuous Si-rich oxide layer and prevent the internal oxidation. Therefore, higher amount of Si (> 1.0 wt%) might be required for a continuous Si-rich oxide layer formation at the investigated temperature range.

5. Conclusions

Based on the experimental results, the following conclusions can be obtained:

(a) Instead of a triple oxide layer structure (Fe_3O_4-$FeCr_2O_4$-IOZ), the oxide layer formed on 9 wt.% Cr ferritic/martensitic steels (Si alloyed) consist of an outer spinel layer ($FeCr_2O_4$) plus an IOZ. Due to the relatively large surface area of exposed samples and limited oxygen diffusion from cover gas to liquid LBE, the oxygen content dissolved in molten LBE probably dropped to a value below 10^{-6} wt.%, which is insufficient to stabilize the Fe_3O_4 at 550 and 600 °C.

(b) The growth rate of spinel layer is significantly reduced by adding Si (0.7 wt.%, 1.0 wt.%) when the samples are exposed at 550 and 600 °C, or the exposure time prolongs from 1000 to 2000 h. However, the internal oxidation is enhanced by adding Si.

(c) Two SIMP steels (0.7Si, 1.0Si) are able to partially form a Si-rich oxide layer underneath the spinel layer after 2000 h exposure at 600 °C, which might impede the internal oxidation.

(d) Si addition improves the oxide scale adherence in terms of the reduced density of cracks and scale exfoliations. This is mainly attributed to the thinner spinel layer formation.

Data availability

The raw/processed data required to reproduce these findings cannot be shared at this time due to technical or time limitations.
The datasets obtained during the current study are available from the corresponding author on reasonable request.

Acknowledgements

This work is supported by the Helmholtz program NUSAFE at the Karlsruhe Institute of Technology and has been carried out in the frame of EERA Point Programme of Nuclear Materials. H. Wang acknowledges the funding from the National Natural Science Foundation of China (NSFC) [Grant No. 12175221, 52122103, U1967211]. K.L Wang acknowledges the funding from the National Natural Science Foundation of China (51861135315). Hao Shi appreciates the Postdoc fellowship jointly funded by Helmholtz-OCPC Program (No. 20191028).

Reference

[1] C. Fazio, V.P. Sobolev, A. Aerts, S. Gavrilov, K. Lambrinou, P. Schuurmans, A. Gessi, P. Agostini, A. Ciampichetti, L. Martinelli, S. Gosse, Handbook on lead-bismuth eutectic alloy and lead properties, materials compatibility, thermal-hydraulics and technologies-2015 edition (No. NEA--7268), Organisation for Economic Co-Operation and Development, 2015.

[2] V.P. Sobolev, P. Schuurmans, G. Benamati, Thermodynamic properties and equation of state of liquid lead and lead–bismuth eutectic, J. Nucl. Mater. 376 (2008) 358-362, https://doi.org/10.1016/j.jnucmat.2008.02.030.

[3] V. Sobolev, Database of thermophysical properties of liquid metal coolants for GEN-IV, Scientific Report SCIENTIFIC REPORT SCK•CEN-BLG-1069, Mol Belgium, ISSN 1379-2407, 2011.

[4] F. Roelofs, B. de Jager, A. Class, H. Jeanmart, P. Schuurmans, A. Ciampichetti, G. Gerbeth, R. Stieglitz, C. Fazio, European research on HLM thermal hydraulics for ADS applications, J. Nucl. Mater. 376 (2008) 401-404, https://doi.org/10.1016/j.jnucmat.2008.02.014.

[5] Z. Su'ud, H. Sekimoto, Design and safety aspect of lead and lead-bismuth cooled long-life small safe fast reactors for various fore configurations, J. Nucl. Sci. Technol. 32 (1995) 834-845, https://doi.org/10.1080/18811248.1995.9731785.

[6] D. Frazer, E. Stergar, C. Cionea, P. Hosemann, Liquid metal as heat transport fluid for thermal solar power applications, Energy Procedia 49 (2014) 627-636, https://doi.org/10.1016/j.egypro.2014.03.068.

[7] J. Pacio, T. Wetzel, Assessment of liquid metal technology status and research paths for their use as efficient heat transfer fluids in solar central receiver systems, Sol. Energy 93 (2013) 11-22, https://doi.org/10.1016/j.solener.2013.03.025.

[8] G. Muller, G. Schumacher, F. Zimmermann, Investigation on oxygen controlled liquid lead corrosion of surface treated steels, J. Nucl. Mater. 278 (2000) 85-95. https://doi.org/10.1016/S0022-3115(99)00211-1.

[9] G. Müller, A. Heinzel, J. Konys, G. Schumacher, A. Weisenburger, F. Zimmermann, V. Engelo, A. Rusanov, V. Markov, Behaviour of steels in flowing liquid PbBi eutectic alloy at 420–600 °C after 4000–7200 h, J. Nucl. Mater. 335 (2004) 163-168, https://doi.org/10.1016/j.jnucmat.2004.07.010.

[10] A. Weisenburger, C. Schroer, A. Jianu, A. Heinzel, J. Konys, H. Steiner, G. Müller, C. Fazio, A. Gessi, S. Babayan, A. Kobzova, Long term corrosion on T91 and AISI1 316L steel in flowing lead alloy and corrosion protection barrier development: Experiments and models, J. Nucl. Mater. 415 (2011) 260-269, https://doi.org/10.1016/j.jnucmat.2011.04.028.

[11] H. Shi, A. Jianu, A. Weisenburger, C. Tang, A. Heinzel, R. Fetzer, F. Lang, R. Stieglitz, G. Müller, Corrosion resistance and microstructural stability of austenitic Fe–Cr–Al–Ni model alloys exposed to oxygen-containing molten lead, J. Nucl. Mater. 524 (2019) 177-190, https://doi.org/10.1016/j.jnucmat.2019.06.043.

[12] H. Shi, R. Fetzer, C.C. Tang, D.V. Szabó, S. Schlabach, A. Heinzel, A. Weisenburger, A. Jianu, G. Müller, The influence of Y and Nb addition on the corrosion resistance of Fe-Cr-Al-Ni model alloys exposed to oxygen-containing molten Pb, Corros. Sci. 179 (2020) 109152, https://doi.org/10.1016/j.corsci.2020.109152.

[13] C. Schroer, O. Wedemeyer, J. Novotny, A. Skrypnik, J. Konys, Selective leaching of nickel and chromium from Type 316 austenitic steel in oxygen-containing lead–bismuth eutectic (LBE), Corros. Sci. 84 (2014) 113-124, https://doi.org/10.1016/j.corsci.2014.03.016.

[14] A. Weisenburger, A. Jianu, S. Doyle, M. Bruns, R. Fetzer, A. Heinzel, M. DelGiacco, W. An, G. Müller, Oxide scales formed on Fe–Cr–Al-based model alloys exposed to oxygen containing molten lead, J. Nucl. Mater. 437 (2013) 282–292, https://doi.org/10.1016/j.jnucmat.2013.02.044.

[15] J. Lim, I.S. Hwang, J. H. Kim, Design of alumina forming FeCrAl steels for lead or lead–bismuth cooled fast reactors, J. Nucl. Mater. 441 (2013) 650-660, https://doi.org/10.1016/j.jnucmat.2012.04.006.

[16] F. Barbier, A. Rusanov, Corrosion behavior of steels in flowing lead–bismuth, J. Nucl. Mater. 296 (2001) 231-236, https://doi.org/10.1016/S0022-3115(01)00521-9.

[17] M. P. Short, R. G. Ballinger, H. E. Hänninen, Corrosion resistance of alloys F91 and Fe–12Cr–2Si in lead–bismuth eutectic up to 715 °C, J. Nucl. Mater. 434 (2013) 259-281,

https://doi.org/10.1016/j.jnucmat.2012.11.010.
[18] C. Schroer, V. Koch, O. Wedemeyer, A. Skrypnik, J. Konys, Silicon-containing ferritic/martensitic steel after exposure to oxygen-containing flowing lead–bismuth eutectic at 450 and 550 °C, J. Nucl. Mater. 469 (2016) 162-176, https://doi.org/10.1016/j.jnucmat.2015.11.058.
[19] Y. Kurata, Corrosion behavior of Si-enriched steels for nuclear applications in liquid lead–bismuth, J. Nucl. Mater. 437 (2013) 401-408, https://doi.org/10.1016/j.jnucmat.2013.02.022.
[20] J. Wang, S. Lu, L. Rong, D. Li, Y. Li, Effect of silicon on the oxidation resistance of 9 wt.% Cr heat resistance steels in 550 °C lead-bismuth eutectic, Corros. Sci. 111 (2016) 13-25, https://doi.org/10.1016/j.corsci.2016.04.020.
[21] Q. Shi, J. Liu, H. Luan, Z. Yang, W. Wang, W. Yan, Y. Shan, K. Yang, Oxidation behavior of ferritic/martensitic steels in stagnant liquid LBE saturated by oxygen at 600 °C, J. Nucl. Mater. 457 (2015) 135-141, https://doi.org/10.1016/j.jnucmat.2014.11.018.
[22] Y. Zhang, H. He, H. Wang, G. Chen, X. An, Y. Wang, Evolution of microstructure and mechanical properties of 9Cr ferrite/martensite steels with different Si content after long-term aging at 550 °C, J. Alloys Compd. (2021) 159817, https://doi.org/10.1016/j.jallcom.2021.159817.
[23] J. Liu, Q. Shi, H. Luan, W. Yan, W. Sha, W. Wang, Y. Shan, K. Yang, Oxidation and tensile behavior of ferritic/martensitic steels after exposure to lead-bismuth eutectic, Mater. Sci. Eng. A 670 (2016) 97-105, https://doi.org/10.1016/j.msea.2016.05.100.
[24] J. Liu, W. Yan, W. Sha, W. Wang, Y. Shan, K. Yang, Effects of temperature and strain rate on the tensile behaviors of SIMP steel in static lead bismuth eutectic, J. Nucl. Mater. 473 (2016) 189-196, https://doi.org/10.1016/j.jnucmat.2016.02.032.
[25] C. F. Old, Liquid metal embrittlement of nuclear materials, J. Nucl. Mater. 92 (1980) 2-25, https://doi.org/10.1016/0022-3115(80)90136-1.
[26] T. Auger, Z. Hamouche, L. Medina-Almazan, D. Gorse, Liquid metal embrittlement of T91 and 316L steels by heavy liquid metals: A fracture mechanics assessment, J. Nucl. Mater. 377 (2008) 253-260, https://doi.org/10.1016/j.jnucmat.2008.02.043.
[27] X. Gong, J. Chen, F. Hu, C. Xiang, Z. Yu, J. Xiao, H. Wang, H. Gong, H. Wang, C. Liu, Y. Deng, B. Pang, X. Huang, Y. Li, Y. Yin, Liquid metal embrittlement of an Fe10Cr4Al ferritic alloy exposed to oxygen-depleted and-saturated lead-bismuth eutectic at 350 °C, Corros. Sci. 165 (2020) 108364, https://doi.org/10.1016/j.corsci.2019.108364.
[28] J. Van den Bosch, R.W. Bosch, D. Sapundjiev, A. Almazouzi, Liquid metal embrittlement susceptibility of ferritic–martensitic steel in liquid lead alloys, J. Nucl. Mater. 376 (2008) 322-329, https://doi.org/10.1016/j.jnucmat.2008.02.008.
[29] C. Ye, J. B. Vogt, I. P. Serre, Liquid metal embrittlement of the T91 steel in lead bismuth eutectic: The role of loading rate and of the oxygen content in the liquid metal, Mater. Sci. Eng. A 608 (2014) 242-248, https://doi.org/10.1016/j.msea.2014.04.082.
[30] G. Müller, A. Heinzel, G. Schumacher, A. Weisenburger, Control of oxygen concentration in liquid lead and lead–bismuth, J. Nucl. Mater. 321 (2003) 256-262, https://doi.org/10.1016/S0022-3115(03)00250-2.
[31] J. Zhang, Oxygen control technology in applications of liquid lead and lead–bismuth systems for mitigating materials corrosion, J. Appl. Electrochem. 43 (2013) 755-771, DOI 10.1007/s10800-013-0568-8.
[32] C. Schroer, Z. Voß, O. Wedemeyer, J. Novotny, J. Konys, Oxidation of steel T91 in flowing lead–bismuth eutectic (LBE) at 550 °C, J. Nucl. Mater. 356 (2006) 189-197, https://doi.org/10.1016/j.jnucmat.2006.05.009.

[33] V. Tsisar, C. Schroer, O. Wedemeyer, A. Skrypnik, J. Konys, Characterization of corrosion phenomena and kinetics on T91 ferritic/martensitic steel exposed at 450 and 550 °C to flowing Pb-Bi eutectic with 10^{-7} mass% dissolved oxygen, J. Nucl. Mater. 494 (2017) 422-438, https://doi.org/10.1016/j.jnucmat.2017.07.031.

[34] C. Schroer, Guidelines for Corrosion Testing in Liquid Metals (Pb, LBE), MATTER Project, deliverable report D3.4, (2011-2015), 26 (accessed 01/05/2021), http://www.eera-jpnm.eu/filesharer/documents/_Euratom_Projects/Past%20projects/MATTER%20public%20deliverables/Deliverable%20D3.4%20MATTER.pdf.

[35] A. Atkinson, A theoretical analysis of the oxidation of Fe-Si alloys, Corros. Sci. 22 (1982) 87-102, https://doi.org/10.1016/0010-938X(82)90071-3.

[36] C. Schroer, O. Wedemeyer, J. Novotny, A. Skrypnik, J. Konys, Performance of 9% Cr steels in flowing lead-bismuth eutectic at 450 and 550 °C, and 10^{-6} mass% dissolved oxygen, Nucl. Eng. Des. 280 (2014) 661-672, https://doi.org/10.1016/j.nucengdes.2014.01.023.

[37] C. Schroer, V. Koch, O. Wedemeyer, A. Skrypnik, J. Konys, Silicon-containing ferritic/martensitic steel after exposure to oxygen-containing flowing lead–bismuth eutectic at 450 and 550 °C, J. Nucl. Mater. 469 (2016) 162-176, https://doi.org/10.1016/j.jnucmat.2015.11.058.

[38] P. Tunthawiroon, Y. Li, N. Tang, Y. Koizumi, A. Chiba, Effects of alloyed Si on the oxidation behaviour of Co–29Cr–6Mo alloy for solid-oxide fuel cell interconnects, Corros. Sci. (2015) 95, 88-99, https://doi.org/10.1016/j.corsci.2015.02.036.

[39] I. G. Wright, M. Schutze, P. F. Tortorelli, R. B. Dooley, Towards improved prediction of scale exfoliation from steam tubes, Mater. at High Temp. 24 (2007) 265-274, https://doi.org/10.3184/096034007X277933.

[40] L. Martinelli, T. Dufrenoy, K. Jaakou, A. Rusanov, F. Balbaud-Célérier, High temperature oxidation of Fe–9Cr–1Mo steel in stagnant liquid lead–bismuth at several temperatures and for different lead contents in the liquid alloy, J. Nucl. Mater. 376 (2008) 282-288, https://doi.org/10.1016/j.jnucmat.2008.02.006.